

# Numerical analysis of the performance of a venturi-shaped roof for natural ventilation: influence of building width

T. van Hooff \*<sup>(a,b)</sup>, B. Blocken<sup>(a)</sup>, L. Aanen<sup>(c)</sup>, B. Bronsema<sup>(d)</sup>

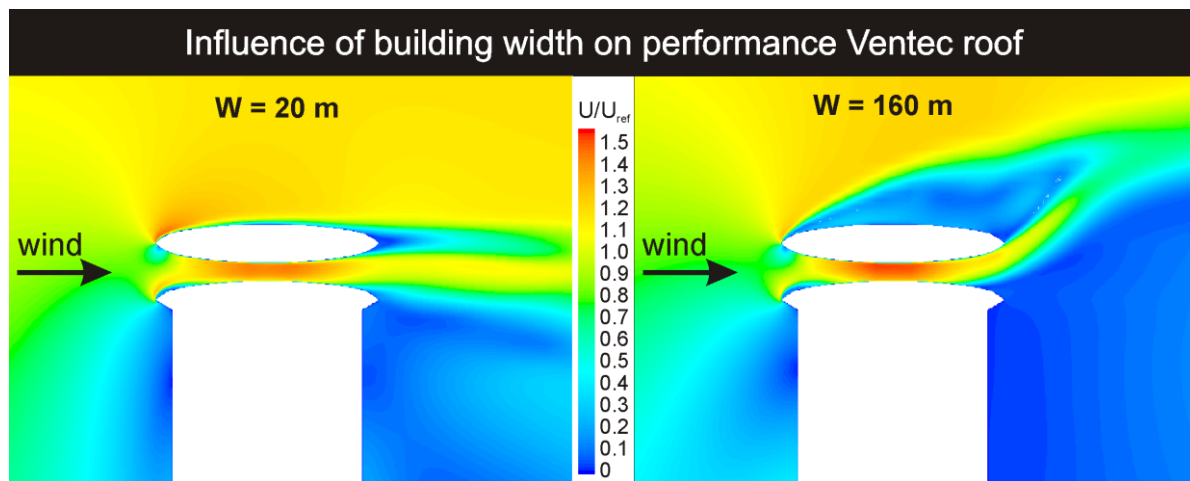
(a) *Building Physics and Services, Eindhoven University of Technology, P.O. box 513, 5600 MB Eindhoven, the Netherlands*

(b) *Division of Building Physics, Department of Civil Engineering, Katholieke Universiteit Leuven, Kasteelpark Arenberg 40, P.O. Box 2447, 3001 Leuven, Belgium*

(c) *Peutz BV, P.O. box 66, 6585 ZH, Mook, The Netherlands*

(d) *Faculty of Architecture – Department of Climate Design, Delft University of Technology, Prof. Boerhaaveweg 37, 2251 HX Voorschoten, The Netherlands*

## Graphical abstract



## Highlights

- Venturi-shaped roof can improve natural ventilation potential of buildings
- Building geometry influences roof performance
- 3D steady RANS study of influence of building width on roof performance
- Five building widths tested: 20, 40, 80, 120, 160 m
- Increasing building width leads to increased performance due to changed static pressure fields

\* **Corresponding author:** Twan van Hooff, Building Physics and Services, Eindhoven University of Technology, P.O.Box 513, 5600 MB Eindhoven, the Netherlands. Tel.: +31 (0)40 247 5877, Fax +31 (0)40 243 8595  
E-mail address: t.a.j.v.hooff@tue.nl

# Numerical analysis of the performance of a venturi-shaped roof for natural ventilation: influence of building width

T. van Hooff \*<sup>(a,b)</sup>, B. Blocken<sup>(a)</sup>, L. Aanen<sup>(c)</sup>, B. Bronsema<sup>(d)</sup>

(a) *Building Physics and Services, Eindhoven University of Technology, P.O. box 513, 5600 MB Eindhoven, the Netherlands*

(b) *Division of Building Physics, Department of Civil Engineering, Katholieke Universiteit Leuven, Kasteelpark Arenberg 40, P.O. Box 2447, 3001 Leuven, Belgium*

(c) *Peutz BV, P.O. box 66, 6585 ZH, Mook, The Netherlands*

(d) *Faculty of Architecture – Department of Climate Design, Delft University of Technology, Prof. Boerhaaveweg 37, 2251 HX Voorschoten, The Netherlands*

## Abstract

A numerical analysis with Computational Fluid Dynamics (CFD) is performed to investigate the influence of building width on the performance of a venturi-shaped roof (called Ventec roof) for natural ventilation. The specific roof configuration is intended to create an underpressure in the narrowest roof section (contraction) which can be used to partly or completely drive the natural ventilation of the building zones. In previous studies, the influence of the roof configuration on its performance was analysed in detail, however these studies were all performed for a fixed building geometry, i.e. a tower building with floor plan 20 x 20 m<sup>2</sup> and a height of 50 m. It is important to analyse the performance of the Ventec roof for different building widths. Therefore, the present paper presents CFD simulations for building (and roof) widths of 20, 40, 80, 120 and 160 m. The 3D steady Reynolds-averaged Navier-Stokes (RANS) approach with the Renormalization Group (RNG) k- $\epsilon$  model is used. The simulations are based on grid-sensitivity analysis and on validation by comparison with wind tunnel experiments. The simulations show that the aerodynamic performance of the roof in terms of the underpressure in the contraction improves with 31% when the building width is increased from 20 m to 40 m, while further increasing the building width only provides relatively small additional improvements. The increased performance with increasing building width is attributed to the larger overpressure upstream of the building and to the larger underpressure and larger size (height) of the wake behind the building.

**Keywords:** Computational Fluid Dynamics (CFD); building dimensions; natural ventilation; venturi-effect; buildings; airflow

## 1. Introduction

Natural ventilation or hybrid natural-mechanical ventilation of buildings can be used to provide a comfortable and healthy indoor environment with reduced energy consumption. Natural ventilation is based on either wind-induced pressure differences or thermally-induced pressure differences, or – most often – a combination of both (Linden 1999, Hunt and Linden 1999, Li and Delsante 2001, Larsen and Heiselberg 2008, Chen 2009, van Hooff and Blocken 2010, Bronsema 2010). The potential for natural ventilation can be significantly enhanced by the design of the building. Because the highest wind speeds are often present at building roof level, in particular the roof geometry can be employed to enhance natural ventilation. This reasoning has driven the design of a specific venturi-shaped roof by Bronsema in the framework of the research project “Earth, Wind & Fire – Air-conditioning powered by Nature” (Bronsema 2010) (Fig. 1). This roof is called the Ventec roof. It consists of a disk-shaped roof construction that is positioned at a certain height above the actual building, creating a contraction that is expected to provide significant underpressures due to the so-called Venturi-effect. The underpressure can be used to partly or completely drive the natural ventilation of the building zones. For this purpose, a vertical channel (not shown in Fig. 1) is provided in the centre of the building, which connects point E of the roof contraction with the building zones at each floor.

---

\* **Corresponding author:** Twan van Hooff, Building Physics and Services, Eindhoven University of Technology, P.O.Box 513, 5600 MB Eindhoven, the Netherlands. Tel.: +31 (0)40 247 5877, Fax +31 (0)40 243 8595  
E-mail address: t.a.j.v.hooff@tue.nl

In a previous paper (van Hooff et al. 2011), the present authors provided a first analysis of the aerodynamic performance of this roof design by CFD and wind tunnel experiments. At this stage, it was found that adding vertical guiding vanes in the roof contraction actually did not improve but cancelled the effect of the contraction. Additional research (Blocken et al. 2011) indicated that due to the guiding vanes, the flow resistance through the contraction became too large and that therefore the oncoming wind would flow over and around the roof and the building, rather than being forced to flow between and along the guiding vanes in the contraction. This phenomenon was called the “wind-blocking effect” in earlier studies (Blocken et al. 2007a, 2008a, 2008b). To further optimize the roof performance, the venturi-effect and the wind-blocking effect were analysed in detail as a function of the roof contraction height and the contraction ratio (Blocken et al. 2011). However, these studies were all performed for a fixed building geometry, i.e. a tower building with floor plan 20 x 20 m<sup>2</sup> and a height of 50 m. It is not clear how the building geometry influences the performance of the roof, therefore it is important to analyse the performance of the Ventec roof for different building widths.

In the present study, 3D steady Reynolds-averaged Navier-Stokes (RANS) CFD with the Renormalization Group (RNG)  $k$ - $\epsilon$  model is used to investigate the influence of the building width on the performance of the roof, in terms of the underpressure in the contraction. Simulations are performed for building widths of 20, 40, 80, 120 and 160 m. Also the width of the roof is adjusted, to match the building width. Section 2 describes the building and roof geometry. Section 3 presents the CFD analysis for the basic configuration, including the grid-sensitivity analysis and the validation with the wind tunnel experiments. In section 4, the influence of the building width on the roof performance is analysed. Finally, sections 5 (discussion) and 6 (conclusions) conclude the paper.

## 2. Description of building and roof geometry

Figure 1 illustrates the basic geometry of the building with the venturi-shaped roof. The building has a rectangular (20 x 20 m<sup>2</sup>) floor plan and a height of 50 m, measured up to the edge of the roof. The Ventec roof consists of two parts. The lower part is constructed from half a “square disk” with dimensions 23.4 m x 23.4 m x 2 m (L x W x H) and it is positioned directly on top of the building, this way creating a roof overhang of 1.7 m on each side of the building, at which ventilation inlets will be placed. At a distance ‘c’ (contraction height) above this part of the roof a “full square disk” is positioned with dimensions 23.4 m x 23.4 m x 4 m (L x W x H), resulting in a nozzle-shaped roof entrance from all four sides of the building. This part can be supported by a set of slender vertical columns. In the present study, the inlet height  $b = 6$  m and the contraction height  $c = 2$  m. The additional building and roof configurations are generated by applying a geometrical scaling factor to the building and roof width. The scaling factors are 2, 4, 6 and 8, yielding building widths  $W = 40$  m, 80 m, 120 m and 160 m, respectively.

The position of main interest inside the roof contraction is the point in the bottom centre of the roof, indicated with the letter E (from “exhaust”) in Figure 1a and b. In this study, the exhaust is considered to be closed and the surface pressure at this position, as well as at the entire roof surface, will be evaluated. All simulations are conducted for an isolated building, i.e. without surrounding buildings. Therefore, all differences in wind speed and surface pressures between the different geometries are only due to changes in the width of the building and the roof.

## 3. Analysis of roof performance for the basic geometry

### 3.1. Wind tunnel measurements

Wind tunnel measurements were performed to validate the CFD simulations. A reduced-scale model (1:100) of the basic geometry (building width  $W = 20$  m) was tested in the closed-circuit atmospheric boundary layer (ABL) wind tunnel at Peutz BV in Mook, the Netherlands. The dimensions of the wind tunnel test section are 3.2 x 1.8 m<sup>2</sup> (width x height), resulting in a blockage ratio of about 2%. The surface pressure was measured at position E (Fig. 1) with a HCLA12X5EB amplified differential pressure sensor from Sensortech. The wind speed in the roof contraction was measured in the centre of the contraction, at mid-height, using a NTC resistor element. The NTCs are operated with a constant current and are calibrated by Peutz by determining the relationship between wind speed and temperature (and corresponding resistance) of each individual probe. The probes are not direction-sensitive and due to the relatively long reaction time of the probes, only average wind speeds can be measured, with an accuracy of  $\pm 10\%$ . Approach-flow vertical profiles of mean wind speed  $U$  and turbulence intensity  $I_u$  are measured at the edge of the turntable using hot-wire anemometers and are presented in Figure 2. The measured wind speed profile can be described by a logarithmic law with a friction velocity  $u^* = 0.956$  m/s and an aerodynamic roughness length  $y_0 = 0.005$  m (full scale:  $y_0 = 0.5$  m). The incident reference wind speed at roof height (full scale: 50 m; reduced scale: 0.5 m)  $U_{ref}$  is 10.5 m/s. Measurements are made for

four wind directions:  $\varphi = 0^\circ, 15^\circ, 30^\circ$  and  $45^\circ$ , taking into account the symmetry of the building and the venturi-shaped roof.

### 3.2. Computational geometry and grid

The computational domain has (full-scale) dimensions  $L \times B \times H = 1020 \text{ m} \times 1020 \text{ m} \times 300 \text{ m}$  (Fig. 3a). This domain shape allows modelling different wind directions ( $0^\circ$  to  $45^\circ$ ). The distance from the inlet, the lateral boundaries and the top boundary is at least  $5H$  away from the building, with  $H$  the building height ( $= 50 \text{ m}$ ) (Franke et al. 2004, 2007, Tominaga et al. 2008). Franke et al. (2004) recommend a maximal blockage ratio of 3% for buildings with a width that is much larger than the height. The blockage ratio for the case with  $W = 160 \text{ m}$  is 0.3%, which is far below the recommended maximum. The flow field upstream of the building was checked to ensure a proper flow development in this region. The outlet is positioned at a distance of  $15H$  to allow full flow development behind the building. A high-resolution computational grid was constructed based on a grid-sensitivity analysis (see Fig. 3b and Fig. 4). The grid-sensitivity analysis is reported in (van Hooff et al. 2011) and (Blocken et al. 2011). The grid has at least 10 cells between each two adjacent surfaces as requested by the best practice guidelines by Franke et al. (2007) and Tominaga et al. (2008). The grid was generated using the grid generation technique presented by van Hooff and Blocken (2010), by which the geometry and the grid are created simultaneously by a series of extrusion operations. Note that the grids do not contain any pyramidal or tetrahedral cells. A high grid resolution is applied in the proximity of the roof in view of the expected large flow gradients (Fig. 4). The grid has a total of 2,375,016 cells and the  $y^+$  values in the roof contraction are around 2,000.

### 3.3. Boundary conditions

At the inlet of the domain the measured approach-flow mean wind speed profile is imposed. Turbulent kinetic energy  $k$  is calculated from the turbulence intensity  $I_u$  using  $k = 0.5(I_u U)^2$ . The turbulence dissipation rate  $\varepsilon = (u^*)^3/\kappa(y+y_0)$ , where  $y$  is the height coordinate,  $\kappa$  the von Karman constant ( $\kappa = 0.42$ ) and  $u^*$  the friction velocity related to the logarithmic mean wind speed profile. At the ground and building surfaces, the standard wall functions by Launder and Spalding (1974) are used with the sand-grain based roughness modification by Cebeci and Bradshaw (1977). For the ground surface, the parameters  $k_S$  and  $C_S$ , to be used in Fluent (Fluent Inc. 2006) should be selected to represent the rough fetch upstream of the building model. Therefore,  $k_S$  and  $C_S$  have to be determined using their appropriate consistency relationship with  $y_0$ . This relationship was derived by Blocken et al. (2007b) for Fluent and CFX. For Fluent 6, up to at least version 6.3, it is given by  $k_S = 9.793y_0/C_S$ . The combination  $k_S = 0.98 \text{ m}$  and  $C_S = 5$  is selected. The building surfaces are assumed to be smooth ( $k_S = 0 \text{ m}$  and  $C_S = 0.5$ ). Zero static pressure is imposed at the outlet of the domain and the top of the domain is modelled as a slip wall (zero normal velocity and zero normal gradients of all variables).

### 3.4. Solver settings

The 3D steady RANS equations are solved in combination with the RNG  $k$ - $\varepsilon$  turbulence model (Yakhot et al. 1992) using Fluent 6.3.26. The RNG  $k$ - $\varepsilon$  turbulence model was chosen because of its good performance in predicting the surface pressures on the windward building facades and in the roof opening in the previous study (van Hooff et al. 2011) and because of its superior performance in an earlier study by Evola and Popov (2006). Pressure-velocity coupling is taken care of by the SIMPLE algorithm, pressure interpolation is standard and second-order discretization schemes are used for both the convection terms and the viscous terms of the governing equations. Convergence has been monitored carefully and the iterations have been terminated when all scaled residuals showed no further reduction with increasing number of iterations. At this stage, the scaled residuals (Fluent Inc. 2006) were:  $10^{-4}$  for continuity,  $10^{-7}$  for momentum,  $10^{-6}$  for turbulent kinetic energy and  $10^{-4}$  for turbulence dissipation rate.

### 3.5. Results and validation

Figure 5 compares the results from the wind tunnel measurements and the results from the CFD simulations. Figure 5a shows the pressure coefficients  $C_p$  at point E, which are defined as  $C_p = (P - P_0)/(0.5\rho U_{ref}^2)$ , where  $P$  is the local static pressure,  $P_0$  the reference static pressure,  $\rho$  the air density and  $U_{ref}$  the approach-flow wind speed at building height ( $= 50 \text{ m}$ ). Fig. 5b provides a similar comparison for the dimensionless velocity magnitude ( $U/U_{ref}$ ) at mid-height in the centre of the roof contraction. Note that in this ratio,  $U$  is the magnitude of the 3D velocity vector. Figure 5 shows that the aerodynamic performance of the roof is almost independent of the wind direction  $\varphi$ . The differences in measured and simulated values of the pressure coefficients  $C_p$  and the dimensionless velocity magnitudes  $U/U_{ref}$  between the four wind directions  $\varphi$  are in general less than 10%, with

no clear tendency towards an optimal wind direction. In general a good agreement is obtained, where the CFD results are within 10%-15% of the measurements. Based on this validation study, the influence of building width is investigated in the next section.

## 4. Analysis of roof performance for different building widths

### 4.1. Computational settings and parameters

The geometry and the grid for the different building widths are obtained by applying a linear scaling factor along the width of the building. The resulting geometries are shown in Fig. 6. The resulting computational grids are illustrated in Fig. 7. The boundary conditions and solver settings are identical to those outlined in the previous section. However, simulations are only performed for one wind direction, i.e. perpendicular to the wide facade of the building ( $\varphi = 0^\circ$ ).

### 4.2. Results

Fig. 8a displays the pressure coefficient  $C_p$  at point E as a function of the building width  $W$ . When  $W$  increases from 20 m to 40 m, the  $C_p$  value improves (i.e. decreases) with about 31% to a value of -1.24. Further increasing  $W$  leads to additional, but smaller improvements, down to  $C_p = -1.38$  for  $W = 160$  m. Fig. 8b shows the corresponding dimensionless velocity magnitude ( $U/U_{ref}$ ) at mid-height in the centre of the roof contraction. Fig. 9 displays the same parameter  $U/U_{ref}$  in the vertical centre plane through the building. As  $W$  increases, so does the area of low wind speed (stagnation zone) upstream of the building. In addition, also the size (height) of the wake behind the building increases. These observations and their effect on the flow through the roof are more clearly shown in Fig. 10. It appears that the increase of the stagnation zone in front of the building and the increase of the size of the wake and the underpressure value in the wake are responsible for the increase in underpressure at point E and therefore for the improved performance of the roof with increasing building width. Note that the velocity contours in the wake of the building and above the roof of the building do not show a clear trend with increasing width; the direction of the jet that exits the venture-shaped roof as well as the shape of the recirculation zone above the roof vary with building width. The absence of a clear trend in the flow pattern in these regions is the result of a minor oscillatory convergence that was observed for the simulations, which was also reported by Ramponi and Blocken (2012) for a different study. The oscillatory convergence was caused by oscillatory behaviour of the flow pattern in the wake of the building and above the building; slightly different flow patterns were present in these regions depending on the number of iterations before the simulation was terminated. However, these oscillations primarily affected the aforementioned two regions. By monitoring the velocity and pressure inside the roof contraction it was determined that the influence of the oscillatory convergence on the studied parameters inside the roof was negligible; the velocity fluctuations and pressure fluctuations were within 1% and 2% of the mean value, respectively.

Figs. 11a-d show the ratio  $U/U_{ref}$  and the static pressure  $P$  along a horizontal line through the roof contraction, as shown in Fig. 11e. In Figs. 11a-d, the dashed vertical lines mark the positions of the edges of the roof. Figure 11 clearly shows that the increasing building width  $W$  leads to a decrease of the wind speed and to an increase of the overpressure upstream of the roof. The increasing building width  $W$  also leads to a decrease (more negative value) of the underpressure directly downstream of the roof (see Fig. 11d). As a result, the flow through the roof is enhanced and the absolute value of the underpressure is increased.

Although point E appears to be the optimal position for a ventilation exhaust, it is worthwhile to look at the pressure coefficient distribution on the entire lower part of the roof. Figure 12 provides additional information on possible locations of ventilation exhausts. The dashed rectangles in Figure 12 indicate the projected surface areas with low  $C_p$  values. The regions with low  $C_p$  values are defined as the surface areas with  $C_p < -0.8$  for  $W = 20$  m, and  $C_p < -1.1$  for  $W = 40$  m to  $W = 160$  m. The relative surface area ( $A_{C_p < -0.8}/A$ ;  $A_{C_p < -1.1}/A$ ) with low pressures increases with increasing  $W$ ; for  $W = 40$  m 8.2% of the building area has a  $C_p$  value lower than -1.1, while for  $W = 160$  m this percentage is 13.4%. The area with low  $C_p$  values for  $W = 20$  m is 11.8%, but please note that the limit for this building width was set to  $C_p < -0.8$  due to the lower  $C_p$  values, as presented in Figure 8. For  $W = 20$  m, there is not any point in which the underpressure decreases below -1.1. The depth (streamwise direction) of the low-pressure areas varies only slightly with  $W$ : from 29.3% of the entire building depth ( $= 20$  m) for  $W = 40$  m to 33.3% for  $W = 160$  m. The width of the low-pressure areas shows larger variations, ranging from 28% to 40.1% for  $W = 40$  m and  $W = 160$  m, respectively. For  $W = 20$  m, the depth of the low-pressure area is 37.3%, whereas the width is 31.8%. Therefore, the differences between the low-pressure areas can be largely attributed to the increase in width (lateral direction) of the low-pressure area with increasing  $W$ .

## 5. Discussion

The evaluation of the aerodynamic performance of the roof has been mainly conducted based on the value of the pressure coefficient at point E. However, the simulations showed that large pressure gradients are present in the roof contraction. Point E was chosen because of its position in the centre of the contraction, and because it corresponded to the location of the point measurement in the wind tunnel model. A future study on the aerodynamic performance of the roof will include modelling the exhaust flow rate through the vertical channel, and that enters the roof contraction due to the generated underpressure.

The present study only evaluated the influence of building width for wind direction perpendicular to the wide facade of the building. Further research will focus on oblique wind directions, and on the influence of building height and of the approach-flow wind conditions on the performance of the roof.

## 6. Summary and conclusions

This paper has presented a numerical analysis with CFD to investigate the influence of building width on the performance of a venturi-shaped roof for natural ventilation. In previous studies, the influence of the roof configuration on its performance was analysed in detail, however these studies were all performed for a fixed building geometry, i.e. a tower building with a floor plan of 20 x 20 m<sup>2</sup> and a height of 50 m. It was important to analyse the performance of the roof for different building widths. Therefore, the present paper has presented CFD simulations for building (and roof) widths of 20, 40, 80, 120 and 160 m. The 3D steady Reynolds-averaged Navier-Stokes (RANS) approach with the Renormalization Group (RNG) k- $\epsilon$  model were used. The simulations were based on grid-sensitivity analysis and on validation by comparison with wind tunnel experiments. The simulations showed that the aerodynamic performance of the roof in terms of the underpressure in the contraction improved with about 31% when the building width is increased from 20 m to 40 m, while further increasing the building width only provided small additional improvements. The increased performance with increasing building width is attributed to the larger overpressure upstream of the building and to the larger underpressure and larger size (height) of the wake behind the building. The area of the roof which has the potential to contain a ventilation exhaust slightly increases with increasing W; for W = 40 m 9.2% of the roof surface area of the building has a C<sub>p</sub> value lower than -1.1, while for W = 160 m 13.2% of the area has a C<sub>p</sub> value which is lower than -1.1.

## References

- Blocken, B., Carmeliet, J., Stathopoulos, T., 2007a. CFD evaluation of the wind speed conditions in passages between buildings – effect of wall-function roughness modifications on the atmospheric boundary layer flow. *J. Wind Eng. Ind. Aerodyn.* 95(9-11), 941-962.
- Blocken, B., Stathopoulos, T., Carmeliet, J., 2007b. CFD simulation of the atmospheric boundary layer: wall function problems. *Atmos. Environ.* 41(2), 238-252.
- Blocken, B., Stathopoulos, T., Carmeliet, J., 2008a. Wind environmental conditions in passages between two long narrow perpendicular buildings. *J. Aerospace Eng.-ASCE* 21(4), 280-287.
- Blocken, B., Stathopoulos, T., Carmeliet, J., 2008b. A numerical study on the existence of the Venturi-effect in passages between perpendicular buildings. *J. Eng. Mech.-ASCE* 134(12), 1021-1028.
- Blocken, B., van Hooff, T., Aanen, L., Bronsema, B., 2011. Computational analysis of the performance of a venturi-shaped roof for natural ventilation: venturi-effect versus wind-blocking effect. *Comput. Fluids* 48(1), 202-213.
- Bronsema, B., 2010. Earth, Wind & Fire – Air-conditioning powered by nature. 10<sup>th</sup> REHVA World Congress CLIMA 2010, 9-12 May, Antalya, Turkey.
- Cebeci, T., Bradshaw, P., 1977. Momentum transfer in boundary layers, Hemisphere Publishing Corporation.
- Chen, Q., 2009. Ventilation performance prediction for buildings: A method overview and recent applications. *Build. Environ.* 44(4), 848-858.
- Evola, G., Popov, V., 2006. Computational analysis of wind driven natural ventilation in buildings. *Energy Build* 38(5), 491-501.
- Fluent Inc. Fluent 6.3. User's Guide. Fluent Inc., Lebanon; 2006.
- Franke, J., Hirsch, C., Jensen, A.G., Krüs, H.W., Schatzmann, M., Westbury, P.S., Miles, S.D., Wisse, J.A., Wright, N.G., 2004. Recommendations on the use of CFD in wind engineering. In: van Beeck, J.P.A.J. (Ed.), COST Action C14, Impact of Wind and Storm on City Life Built Environment, Proceedings of the International Conference on Urban Wind Engineering and Building Aerodynamics. Von Karman Institute, Sint-Genesius-Rode, Belgium, 5–7 May 2004.
- Franke, J., Hellsten, A., Schlünzen, H., Carissimo, B. (Eds.). 2007. Best practice guideline for the CFD simulation of flows in the urban environment. COST Office Brussels.

- Hunt, G.R., Linden, P.F., 1999. The fluid mechanics of natural ventilation - displacement ventilation by buoyancy-driven flows assisted by wind. *Build. Environ.* 34(6), 707-720.
- Larsen, T.S., Heiselberg, P., 2008. Single-sided natural ventilation driven by wind pressure and temperature difference. *Energy Build.* 40(6), 1031-1040.
- Lauder, B.E., Spalding, D.B., 1974. The numerical computation of turbulent flows. *Comput. Method Appl. M* 3, 269-289.
- Li, Y.G., Delsante, A., 2001. Natural ventilation induced by combined wind and thermal forces. *Build. Environ.* 36(1), 59-71.
- Linden, P.F., 1999. The fluid mechanics of natural ventilation. *Annu. Rev. Fluid Mech.* 31, 201-238.
- Ramponi, R., Blocken, B., 2012. CFD simulation of cross-ventilation for a generic isolated building: Impact of computational parameters. *Build. Environ.* 53: 34-48.
- Tominaga, Y., Mochida, A., Yoshie, R., Kataoka, H., Nozu, T., Yoshikawa, M., Shirasawa, T., 2008. AIJ guidelines for practical applications of CFD to pedestrian wind environment around buildings. *J. Wind Eng. Ind. Aerodyn.* 96(10-11), 1749-1761.
- van Hooff, T., Blocken, B., Aanen, L., Bronsema, B., 2011. A venturi-shaped roof for wind-induced natural ventilation of buildings: wind tunnel and CFD evaluation of different design configurations. *Build. Environ.* 46(9), 1797-1807.
- van Hooff, T., Blocken, B., 2010. Coupled urban wind flow and indoor natural ventilation modelling on a high-resolution grid: A case study for the Amsterdam ArenA stadium. *Environ. Modell. Softw.* 25(1), 51-65.
- Yakhot, V., Orszag, S.A., Thangam, S., Gatski, T.B., Speziale, C.G., 1992. Development of turbulence models for shear flows by a double expansion technique. *Phys. Fluids A4*, 1510-1520.



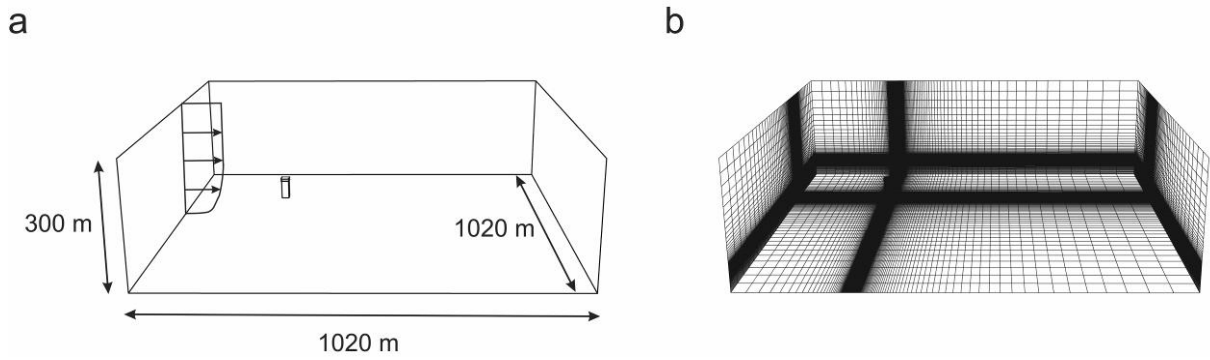


Fig. 3: (a) View of the building in its computational domain (full-scale dimensions). (b) Perspective view of the computational grid at some of the domain surfaces. Total number of cells is 2,375,016.

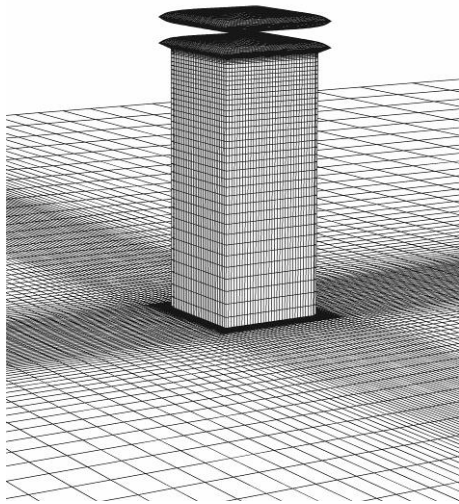


Fig.4: Perspective view of computational grid on the building and ground surfaces. Total number of cells is 2,375,016.

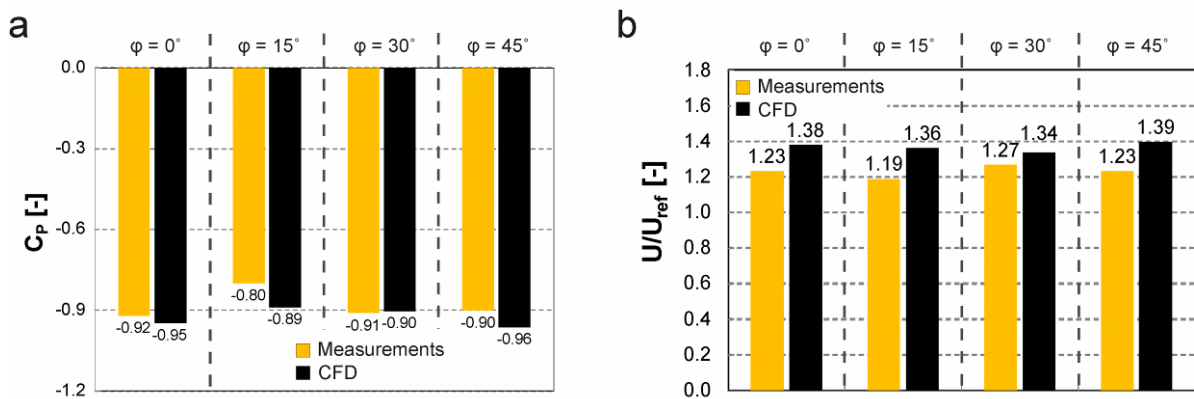


Fig. 5: Comparison of wind tunnel measurements and CFD simulation results for four wind directions ( $\phi = 0^\circ$ ,  $\phi = 15^\circ$ ,  $\phi = 30^\circ$ ,  $\phi = 45^\circ$ ). (a) Pressure coefficient  $C_p$  at point E. (b) Dimensionless velocity magnitude  $U/U_{ref}$  at mid-height in the centre of the roof contraction.  $U_{ref}$  is the approach-flow wind speed at building height (50 m).

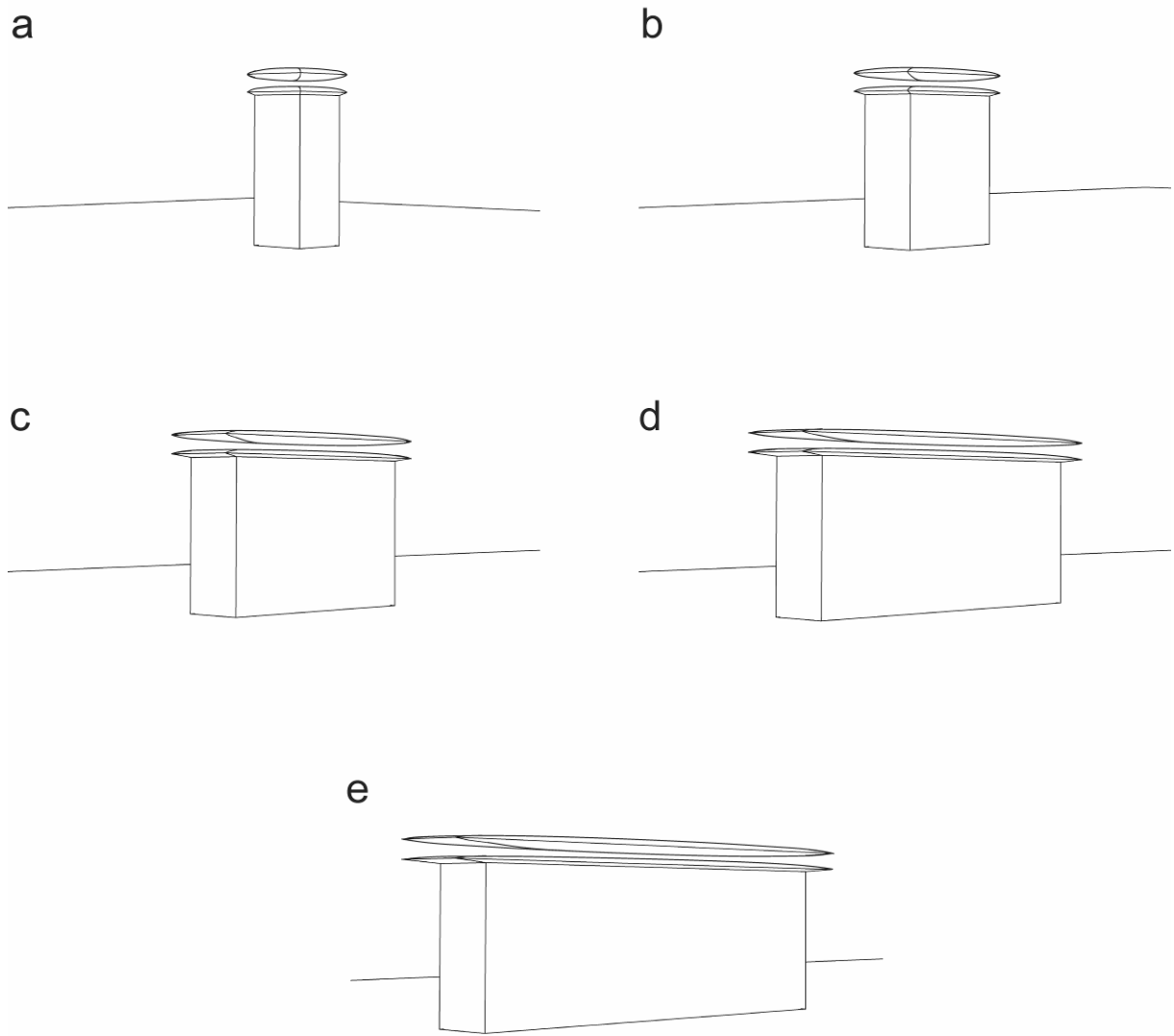


Fig. 6: Five different building and roof geometries: (a)  $W = 20$  m; (b)  $W = 40$  m; (c)  $W = 80$  m; (d)  $W = 120$  m; (e)  $W = 160$  m. The configurations are tested for wind perpendicular to the wide facade.

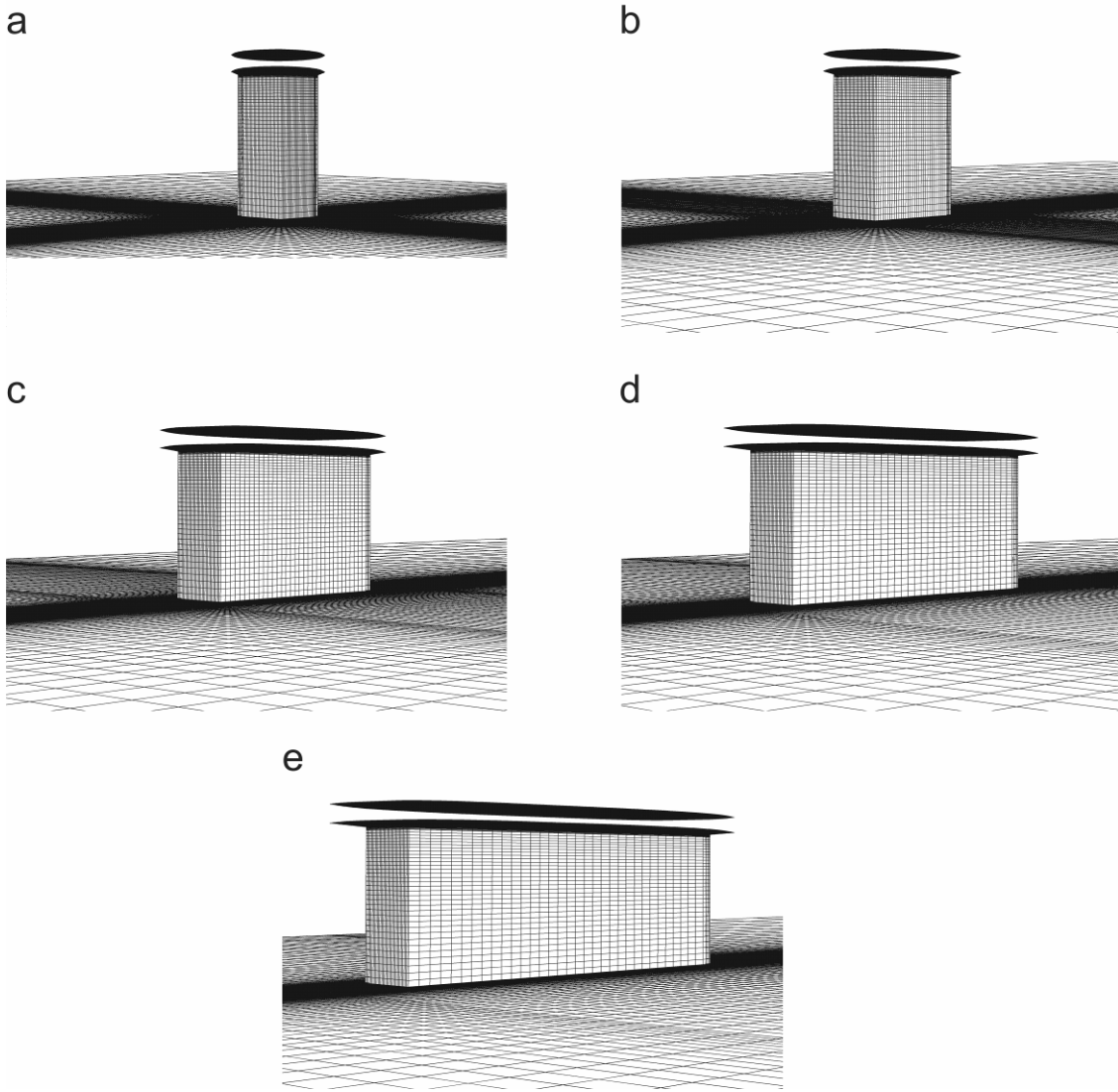


Fig. 7: Computational grids used for the five different building and roof geometries. (a)  $W = 20$  m; (b)  $W = 40$  m; (c)  $W = 80$  m; (d)  $W = 120$  m; (e)  $W = 160$  m. All grids consist of 2,375,016 cells.

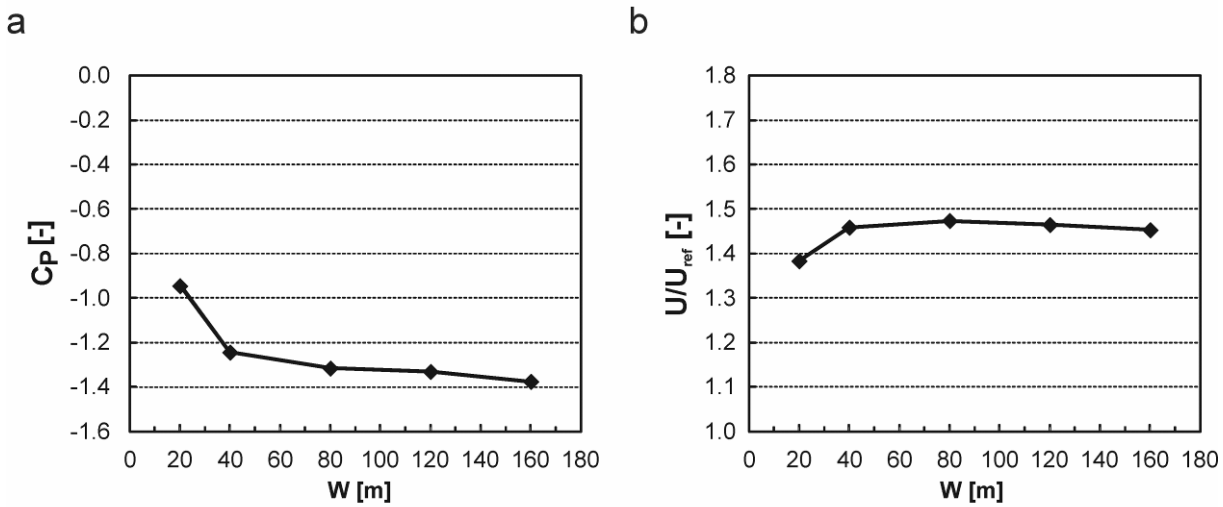


Fig. 8: (a) Wind pressure coefficient  $C_p$  at point E as a function of building width, for wind perpendicular to the wide facade. (b) Dimensionless velocity magnitude ( $U/U_{ref}$ ) at mid-height in the centre of the roof contraction as a function of building width, for wind perpendicular to the wide facade.  $U_{ref}$  is the approach-flow wind speed at building height (50 m).

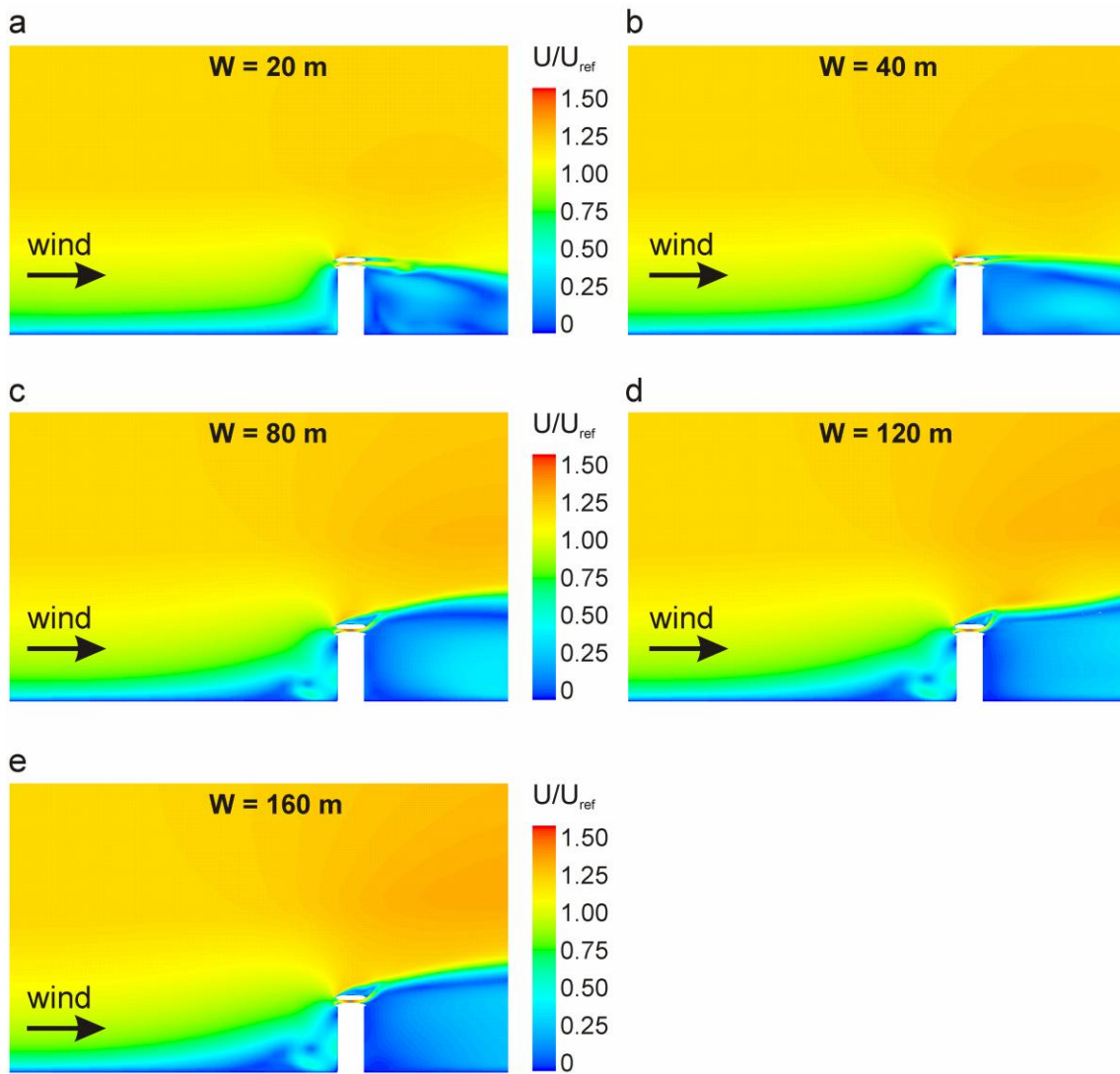


Fig. 9: Contours of dimensionless velocity magnitude ( $U/U_{ref}$ ) in the vertical centre plane through the building, for wind perpendicular to the wide facade. (a)  $W = 20$  m; (b)  $W = 40$  m; (c)  $W = 80$  m; (d)  $W = 120$  m; (e)  $W = 160$  m.  $U_{ref}$  is the approach-flow wind speed at building height (50 m).

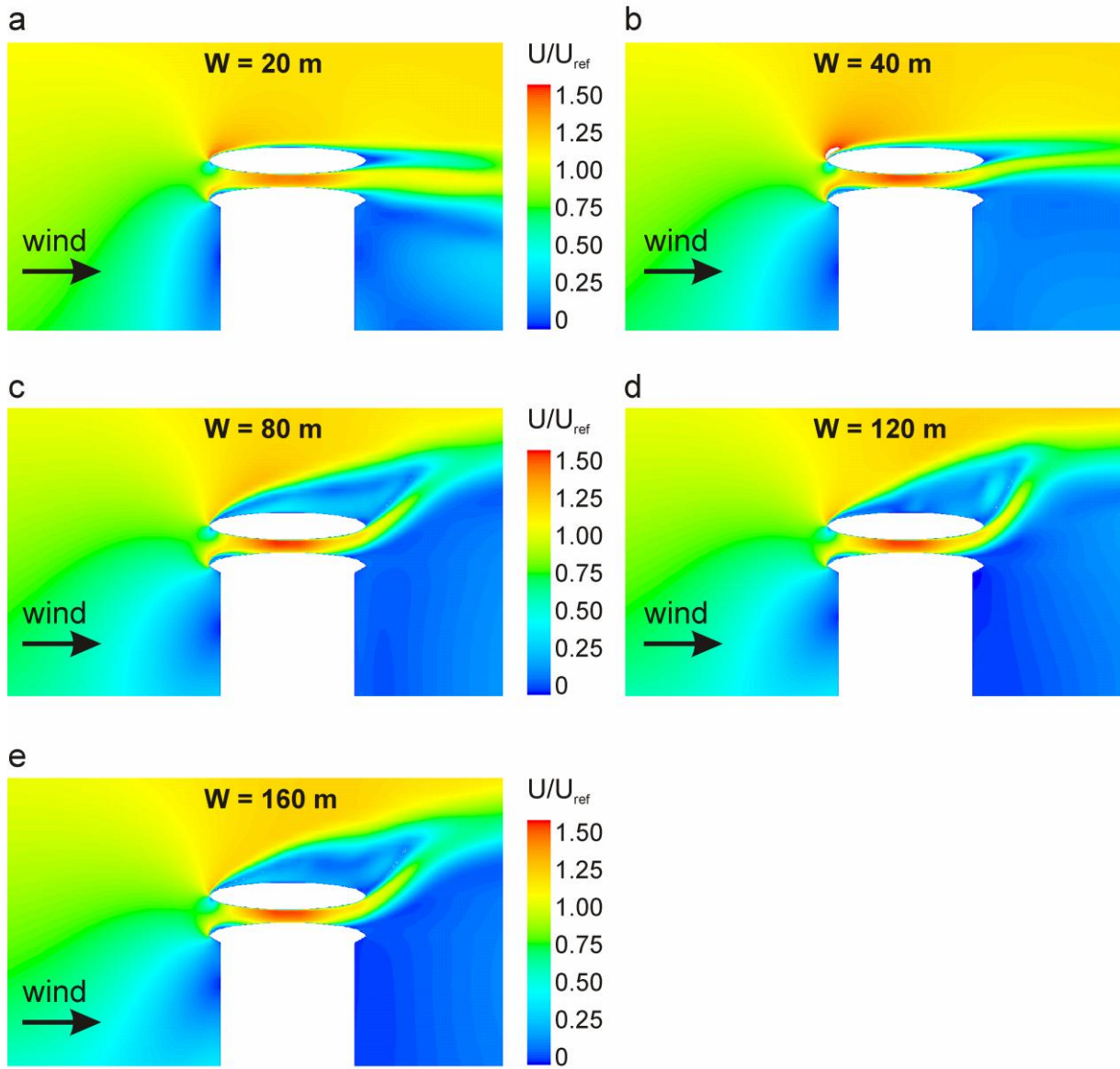


Fig. 10: Enlarged view of contours of dimensionless velocity magnitude ( $U/U_{ref}$ ) in the vertical centre plane through the building, for wind perpendicular to the wide facade. (a)  $W = 20$  m; (b)  $W = 40$  m; (c)  $W = 80$  m; (d)  $W = 120$  m; (e)  $W = 160$  m.  $U_{ref}$  is the approach-flow wind speed at building height (50 m).

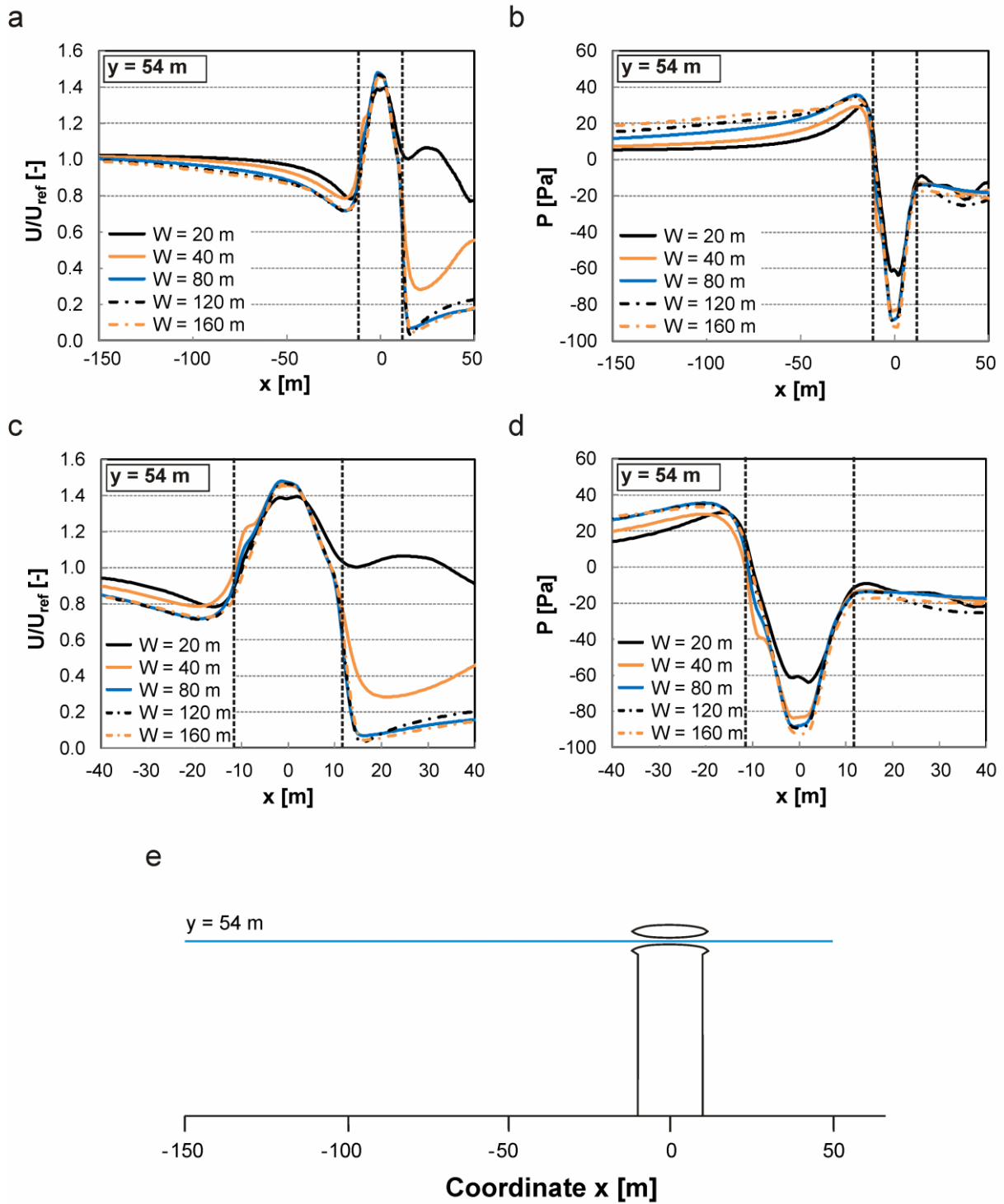


Fig. 11: (a,c) Profiles of dimensionless velocity magnitude ( $U/U_{ref}$ ) upstream and downstream of the building as a function of building width  $W$ , along the plotting line indicated in figure (e). (b,d) Static pressure profiles along the same line. The dashed vertical lines mark the positions of the edges of the roof. (e) Location of the plotting line in the vertical centre plane through the building.

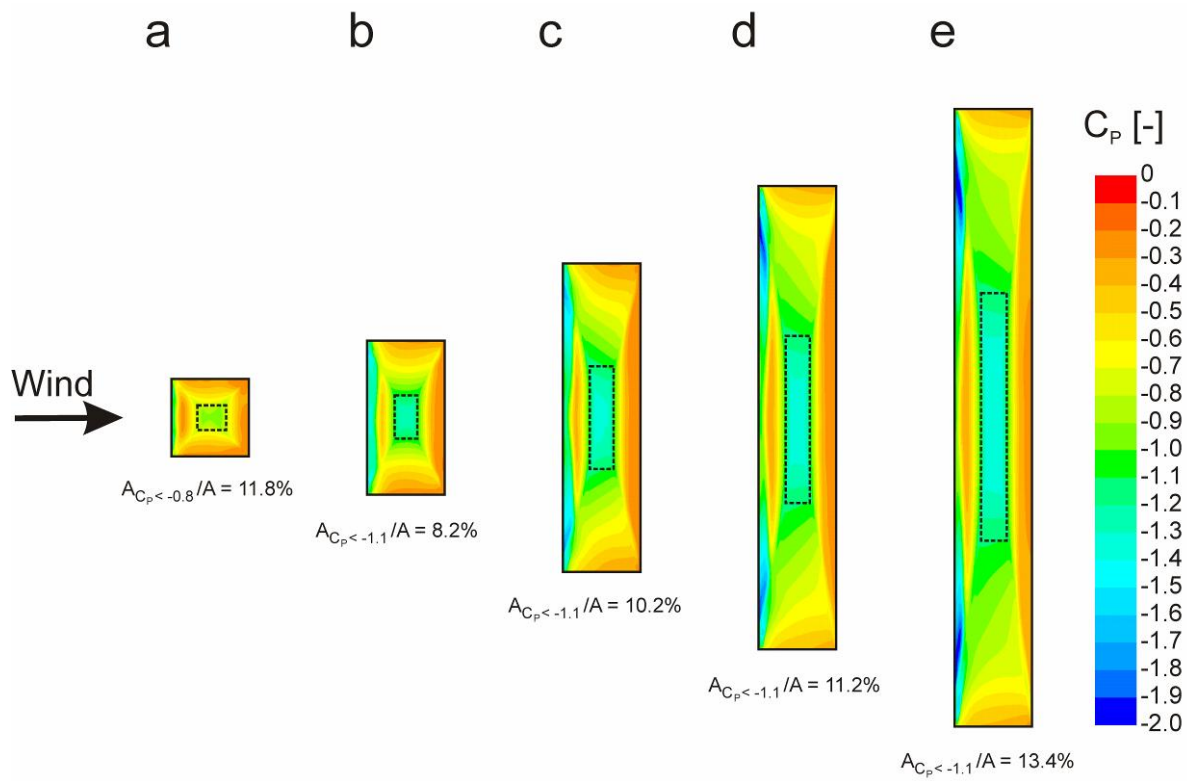


Fig. 12: Contours of the pressure coefficient  $C_p$  at the surface of the lower part of the roof. (a)  $W = 20$  m; (b)  $W = 40$  m; (c)  $W = 80$  m; (d)  $W = 120$  m; (e)  $W = 160$  m.